EIGHTEENTH EUROPEAN ROTORCRAFT FORUM

B - 07

Paper No. 79

UNSTEADY SEPARATED FLOWS ON ROTOR- AIRFOILS
- Analysis and Visualization of Numerical Data-

W.GEISSLER, H.VOLLMERS

DEUTSCHE FORSCHUNGSANSTALT FÜR LUFT- UND RAUMFAHRT,
GÖTTINGEN, GERMANY

September 15-18, 1992

AVIGNON, FRANCE

ASSOCIATION AERONAUTIQUE ET ASTRONAUTIQUE DE FRANCE

Unsteady Separated Flows on Rotor-Airfoils.

-Analysis and Visualization of Numerical Data-

by

W. Geissler, DLR
H.Vollmers, DLR.

Abstract

Unsteady viscous flows with separation may be dominant on retreating rotor blades of helicopters in forward flight. These flows are investigated by a time-accurate numerical solution of the 2d-Navier- Stokes equations on deformable meshes. Lift and moment characteristics are compared with experimental data. Compressibility effects are found to be of considerable importance with respect to the development of the dynamic stall process.

Large sets of field data (i.e. pressure, density, velocities, vorticity, etc) are available to investigate the details of the flow. Suitable visualization techniques are necessary to sufficiently interpret these data. Pseudo 3d-viewing of the 2d-unsteady data as well as the medium: video movie serve as effective tools for physical interpretation and understanding of the unsteady separated flow fields.

1. Introduction:

Unsteady separated flows occur on retreating rotor blades limiting the flight envelope of the helicopter. The details of the unsteady viscous flows involved are still not completely understood. Experimental studies of oscillating rotor blades under separated flow conditions have been discussed in [1].

Experiments are still continuing using new nonintrusive diagnostic measuring techniques like interferometry [2], Laser-Doppler velocimetry [3], etc. In addition to experimental studies, numerical tools and the necessary supercomputers are now available to sufficiently ***calculate*** these flows as well. In recent years unsteady separation has been studied on the basis of coupling procedures between inviscid and viscous parts of the flow [4]. These calculations were continued into regions of reversed flow adjacend to the airfoil surface during upstroke.

But these calculations were limited to dynamic stall ***onset***. The development and shedding of the stall vortex could not be treated by these methods.

The dynamic stall process can only be handled sufficiently on the basis of CFD-methods taking into account the ***complete*** set of viscous equations, i.e. the Navier-Stokes equations. For high Reynolds number flows a corresponding turbulence model must be used.

This extension of numerical efforts to the solution of the complete set of equations has different consequences :

1. A suitable supercomputer must be available, with increasing computation times and costs.
2. Post- processing tools are necessary to be able to interpret the very large amount of numerical data.

In the present paper a short description of the numerical code used for these studies is given. The code is a Beam, Warming-type finite-differencing algorithm [5], with a special treatment of the numerical damping terms necessary for the central difference scheme, [6].

The main emphasis is placed on the comparison of the calculated data with experimental results. Special treatment is focused on the influence of compressibility on the dynamic stall process for different helicopter airfoil sections.

Post-processing procedures and visualization techniques are discussed next for better understanding of the physics of the unsteady separated flow fields involved.

A video movie [7] has been developed showing the dynamic stall process and its influence on various flow quantities like vorticity, pressure and Machnumber in their time-dependent development.

2. Numerical Method.

2.1 Navier-Stokes equations.

For the calculation of the 2d-unsteady flow about airfoils, body fitted curvilinear coordinates ξ , η are used. The Navier-Stokes equations in vector notation read in this system:

$$\frac{\partial \hat{q}}{\partial \tau} + \frac{\partial}{\partial \xi}\hat{E} + \frac{\partial}{\partial \eta}\hat{F} = \frac{1}{Re}\left(\frac{\partial}{\partial \xi}\hat{R} + \frac{\partial}{\partial \eta}\hat{S}\right) \tag{1}$$

with

$$\hat{q} = \frac{1}{J}\begin{bmatrix}\rho\\ \rho u\\ \rho v\\ \rho e_T\end{bmatrix} ; \hat{E} = \frac{1}{J}\begin{bmatrix}\rho U\\ \rho uU + \xi_x p\\ \rho vU + \xi_y p\\ U(\rho e_T + p) - \xi_t p\end{bmatrix} ; \hat{F} = \frac{1}{J}\begin{bmatrix}\rho V\\ \rho uV + \eta_x p\\ \rho vV + \eta_y p\\ V(\rho e_T + p) - \eta_t p\end{bmatrix}$$

and

$$\hat{R} = \frac{1}{J}\begin{bmatrix}0\\ \xi_x\tau_{xx} + \xi_y\tau_{xy}\\ \xi_x\tau_{xy} + \xi_y\tau_{yy}\\ \xi_x R_4 + \xi_y S_4\end{bmatrix} ; \hat{S} = \frac{1}{J}\begin{bmatrix}0\\ \eta_x\tau_{xx} + \eta_y\tau_{xy}\\ \eta_x\tau_{xy} + \eta_y\tau_{yy}\\ \eta_x R_4 + \eta_y S_4\end{bmatrix} \tag{2}$$

U and V are the contravariant velocities.

The transformed viscous terms in (2) are

$$\begin{aligned}
\tau_{xx} &= \mu\left[\frac{4}{3}(\xi_x u_\xi + \eta_x u_\eta) - \frac{2}{3}(\xi_y v_\xi + \eta_y v_\eta)\right]\\
\tau_{xy} &= \mu\left[\xi_y u_\xi + \eta_y u_\eta + \xi_x v_\xi + \eta_x v_\eta\right]\\
\tau_{yy} &= \mu\left[\frac{4}{3}(\xi_y v_\xi + \eta_y v_\eta) - \frac{2}{3}(\xi_x u_\xi + \eta_x u_\eta)\right]\\
R_4 &= u\,\tau_{xx} + v\,\tau_{xy} + \mu\, Pr^{-1}(\gamma - 1)^{-1}\left(\xi_x \partial_\xi a^2 + \eta_x \partial_\eta a^2\right)\\
S_4 &= u\,\tau_{xy} + v\,\tau_{yy} + \mu\, Pr^{-1}(\gamma - 1)^{-1}\left(\eta_y \partial_\xi a^2 + \eta_y \partial_\eta a^2\right)
\end{aligned} \tag{3}$$

ξ_x , ξ_t etc. are the metric terms, J is the Jacobian of the coordinate transformation. The inverse metric terms x_ξ , x_τ , etc. are calculated numerically by central differences. ρ , u , v , a , p , e_T *and* τ in eqs. (2) and (3) have their accustomed meaning.

All terms in eqs.(2),(3) have been made dimensionless with corresponding reference quantities of the undisturbed flow. Re and Pr are the Reynolds and Prandtl number respectively.

2.2 Solution procedure

With the linearization of the different flux vectors (superscript n + 1 refers to the new time step) :

$$\begin{aligned}
\hat{E}^{n+1} &= \hat{E}^n + \left(\partial\hat{E} / \partial\hat{q}\right)^n \Delta\hat{q}^n + O\left(\Delta\tau^2\right)\\
\hat{F}^{n+1} &= \hat{F}^n + \left(\partial\hat{F} / \partial\hat{q}\right)^n \Delta\hat{q}^n + O\left(\Delta\tau^2\right) \quad etc.
\end{aligned} \tag{4}$$

defining $\hat{A} = (\partial\hat{E} / \partial\hat{q})^n$, $\hat{B} = (\partial\hat{F} / \partial\hat{q})^n$ as Jacobian matrices of the flux vectors $\hat{E}$, $\hat{F}$ and corresponding matrices $\hat{K}$, $\hat{L}$ for the viscous fluxes.

Using the approximate factorization implicit solution procedure, [5], the following three steps are carried out:

1. Step (ξ-sweep):

$$\left\{ I + \frac{\Delta\tau}{2} \left[\frac{\partial \hat{A}^n}{\partial \xi} - \frac{\partial^2}{\partial \xi^2} \left(\hat{K} \right)^n \right] \right\} \overline{\Delta \hat{q}^n} = RHS$$

2. Step (η-sweep):

$$\left\{ I + \frac{\Delta\tau}{2} \left[\frac{\partial \hat{B}^n}{\partial \eta} - \frac{\partial^2}{\partial \eta^2} \left(\hat{L} \right)^n \right] \right\} \Delta \hat{q}^n = \overline{\Delta \hat{q}^n} \tag{5}$$

3. Step

$$\hat{q}^{n+1} = \hat{q}^n + \Delta \hat{q}^n$$

with

$$RHS = \Delta\tau \left[\frac{\partial}{\partial \xi} \left(- \hat{E} + \hat{R} \right)^n + \frac{\partial}{\partial \eta} \left(- \hat{F} + \hat{S} \right)^n \right] \tag{6}$$

In the system (5) the implicit viscous terms are retained. The transport coefficients are assumed as locally constant. Viscous cross- derivative terms have been neglected in eq. (6). The latter assumption reduces the order of time-accuracy of the ***viscous terms*** from second order to first order. All spatial derivatives are discretized with second order accuracy.

2.3 Artificial viscosity

Using central differencing in the solution algorithm (5),numerical oscillations may occur due to odd/ even decoupling. Suitable numerical damping terms have to be added to both the implicit and explicit parts of the equations (5),(6). Following the ideas of Pulliam, [6], eigenvalue-scaled dissipation terms are constructed and added to the equations:

The maximum eigenvalues in $\xi -$, $\eta -$ directions are

$$\lambda_\xi = |U| + a\sqrt{\xi_x^2 + \xi_y^2} \quad ; \quad \lambda_\eta = |V| + a\sqrt{\eta_x^2 + \eta_y^2} \tag{7}$$

with a as the local speed of sound.

Using these eigenvalues, second order implicit dissipation terms are formulated:

$$D_{I\,\xi} = - J_{ij}^{-1} \left(\lambda_{\xi\,ij} \nabla_\xi \Delta_\xi J_{ij} \right) \; ; \; D_{I\,\eta} = - J_{ij}^{-1} \left(\lambda_{\eta\,ij} \nabla_\eta \Delta_\eta J_{ij} \right) \tag{8}$$

∇ *and* Δ are the usual backward and forward differencing operators respectively. The terms $D_{I\,\xi}$ *and* $D_{I\,\eta}$ are added to the implicit part, eq. (5).

In a similar way 4th-order explicit terms are formulated and added to the explicit (RHS)-part, eq (6):

$$D_E = D_{E\,\xi} + D_{E\eta}$$

with

$$\begin{aligned} D_{E\,\xi} = & - \nabla_\xi \left[\left(\lambda_{\xi\,i+1,j} J_{i+1,j}^{-1} + \lambda_{\xi\,ij} J_{ij}^{-1} \right) \varepsilon_{ij}^{(2)} \Delta_\xi \hat{q}_{ij}^n \right] \\ & + \nabla_\xi \Delta_\xi \left[\left(\lambda_{\xi\,ij} J_{ij}^{-1} \right) \varepsilon_{ij}^{(4)} \nabla_\xi \Delta_\xi \hat{q}_{ij} \right] \end{aligned} \tag{9}$$

and a corresponding term $D_{E\,\eta}$.

In eq. (9) the different terms are:

$$\varepsilon^{(2)}_{i,j} = k^{(2)} \max\left(\sigma_{i-1,j}, \sigma_{i,j}, \sigma_{i+1,j}\right) \;;\; \sigma_{i,j} = \left| \frac{p_{i+1,j} - 2\,p_{i,j} + p_{i-1,j}}{p_{i+1,j} + 2\,p_{i,j} + p_{i-1,j}} \right| \tag{10}$$

$$\varepsilon^{(4)}_{i,j} = \max\left(0, k^{(4)} - \varepsilon^{(2)}_{i,j}\right) \;;\; k^{(2)} = 0.25 \;,\; k^{(4)} = 1$$

Indices i,j refer to the $i \cdot \Delta\xi$, $j \cdot \Delta\eta$ gridpoint.

Further details of the numerical code and a number of results, comparisons with other methods and with experimental data are given in [8].

2.4 Dynamic mesh generation, types of airfoil motion

The calculation of the unsteady flow fields are carried out in a coordinate mesh which is deforming in time: the mesh is fixed to the airfoil as well as to the outer boundary which is a number of chordlength (10c) away from the airfoil. ***Fig.1*** shows the extreme incidences:

$$\alpha_{min} = 5° \,,\, \alpha_{max} = 25°$$

for a NACA 23012 airfoil section oscillating with $\alpha_1 = 10°$ amplitude about a steady mean angle $\alpha_0 = 15°$. For both cases the mesh has been calculated numerically with the elliptic grid generation procedure of Sorensen [9].

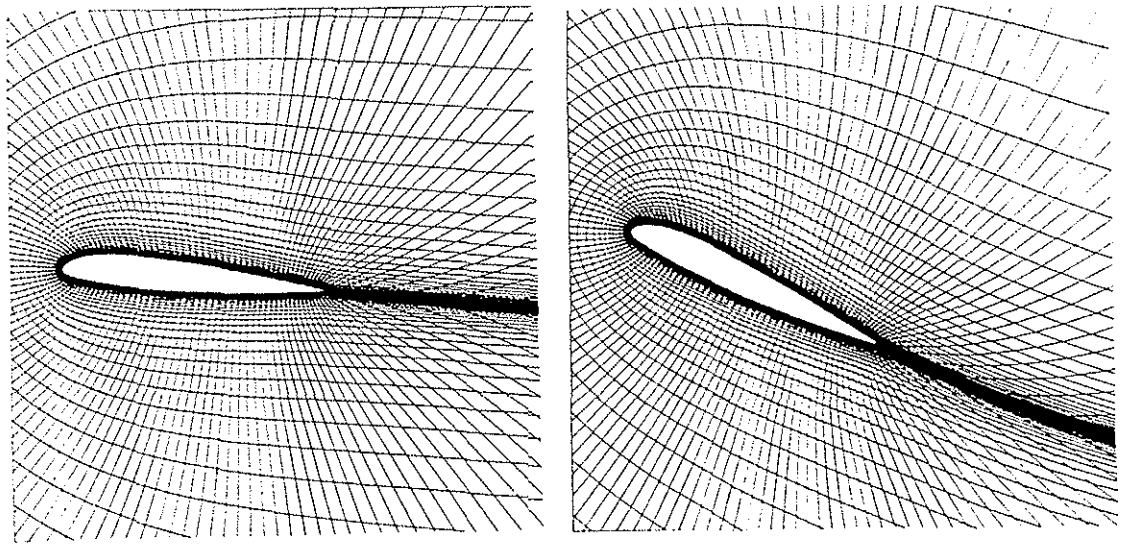

Fig. 1: Grid at minimum (α = 5°, left) and maximum (α = 25°, right) airfoil incidences, NACA 23012

For intermediate time steps a linear interpolation procedure is used, [10]. For simple harmonic motion of the airfoil the inverse metric terms *x, and y,* can be calculated analytically. Two different time-dependent motions of an airfoil:

- sinusoidal pitching motion
- ramp motion

have been realized in the present code. To simulate the flow on a helicopter rotor blade more realistic, a variation of the Machnumber simultaneous to the pitching motion has also been applied.

More complicated time-functions of the airfoil motion as well as arbitrary motions implied by a combination of aerodynamics and structural dynamic constraints (stall flutter) have also been successfully investigated. In these cases the metric time-terms have to be calculated numerically.

3. *Dynamic stall.*

Following the interpretation of McCroskey,[11], the dynamic stall process can be classified into categories: ***Stall onset, light stall, deep stall.*** These different cases depend mainly on the incidence variation of the airfoil. The present paper will concentrate on the deep stall problem, which is characterized by the development and shedding of concentrated vortices from the airfoil surface. The influence of these vortices on lift-, drag- and moment-characteristics are severe.

Several parameters of the flow may influence the start and/ or the strength and shedding histories of the dynamic stall vortex: compressibility effects are of major importance, as will be shown in the next section. Transition from laminar to turbulent flow including a separation bubble has a strong effect. Incidence variation, airfoil shape and Re-number are additional parameters which influence the dynamic stall process considerably. From coupling procedures between boundary layer and potential flow, [4] it is already known, that prior to the development of the stall vortex ***backflow*** exists almost along the complete upper surface of the airfoil. To model these time-dependent reversed flowfields by Navier-Stokes calculations, a corresponding dense mesh is necessary to resolve the flow accurately close to the airfoil surface. The dynamic stall process is strongly influenced by these history effects of the attached boundary layer.

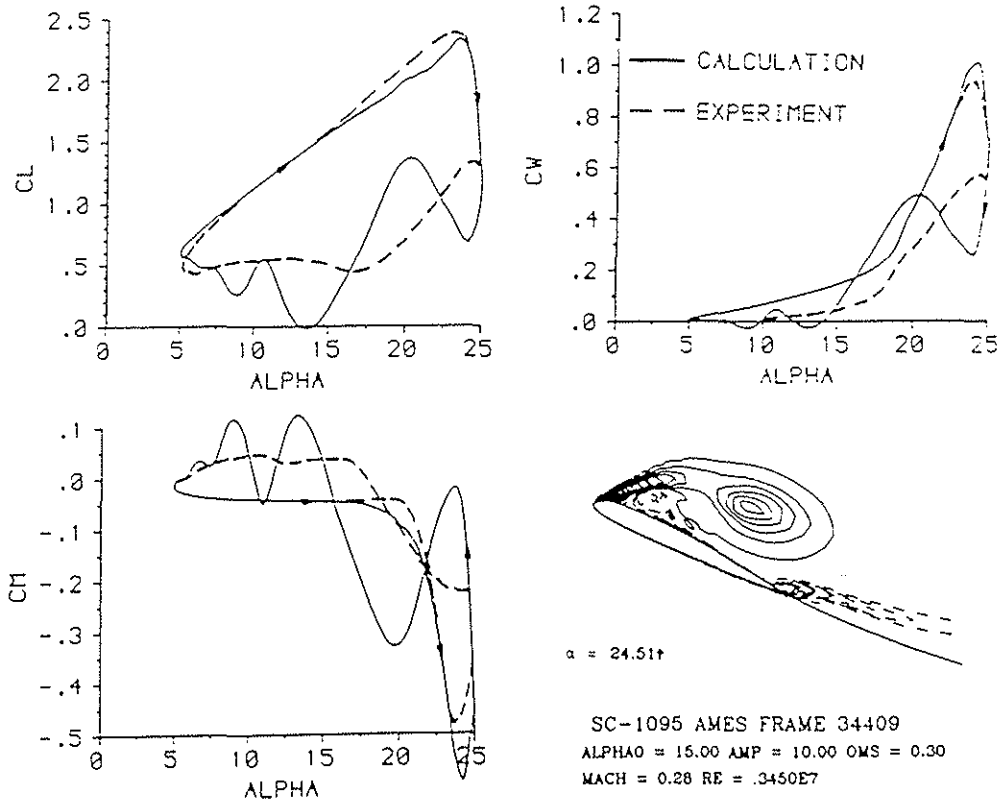

Fig. 2: Force- and moment-distributions for the Sikorsky SC-1095 airfoil section: $Ma_\infty = 0.28$. Instantaneous vorticity distributions at $\alpha = 24.51°$ upstroke.

3.1 Sikorsky SC-1095 airfoil.

Fig. 2 shows numerical and experimental data, [1], for the Sikorsky SC-1095 airfoil section under deep dynamic stall conditions. Strong hysteresis curves are obtained specifically for the lift distribution: In the upstroke region up to $c_{L\,max} \approx 2.4$ the measured and calculated lift values correspond quite well. It must be pointed out, that the maximum ***steady*** lift for this airfoil has been measured as $(c_{L\,max})_{steady} = 1.58$. Before the maximum incidence ($\alpha = 25°$) is reached, the lift breaks down abruptly.

Calculated and measured lift curves show considerable differences in the down stroke region: oscillations are observed for the calculations, however a smooth curve has been measured

Possible explanations for these discrepancies are:

- The experimental data have been assemble averaged over 50 cycles. Oscillations may have been smoothed out.
- The calculations are 2d. In the experiment 3d-vortex structures may occur even on a 2d- model.

Similar hysteresis curves can be observed for the drag- and moment-distributions. Drag rise and moment stall are very good represented by the calculations. Oscillations are also present in these distributions. Of special concern is the behavior of the pitching moment: The areas between the hysteresis curves are a measure of the aerodynamic damping. The sense of traversing these curves determines wether positive (anti-clockwise) or negative (clockwise) damping exsists. If negative damping exceeds, the airfoil may encounter dangerous stall flutter. Fig. 2 shows also the vorticity contours at $\alpha = 24.5°$ upstroke. The stall vortex is already fully developed and has started to lift off the airfoil surface. This corresponds to the breakdown of the lift.

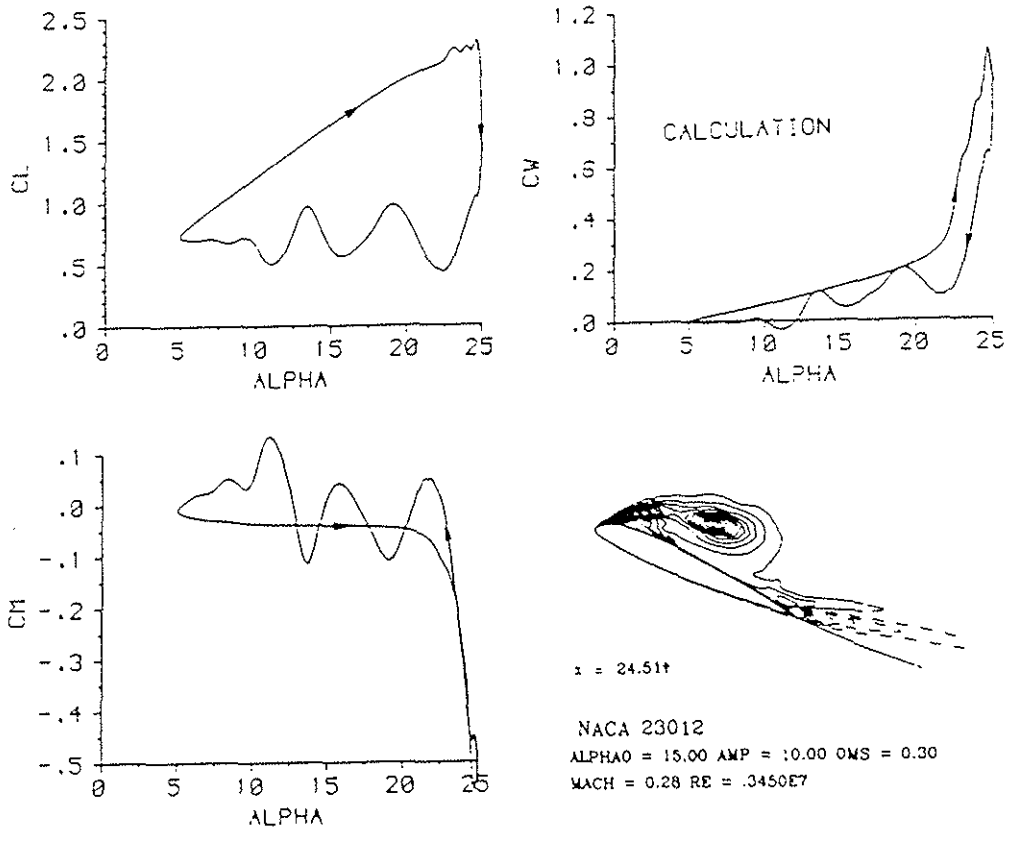

Fig. 3: Force- and moment-distributions for the NACA 23012 airfoil section: $Ma_\infty = 0.28$. Instantaneous vorticity distributions at $\alpha = 24.51°$ upstroke.

3.2 NACA 23012 airfoil.

Fig. 3 shows the corresponding distributions of lift, drag and pitching moment for the NACA 23012 airfoil section. The same parameters are used as in the SC-1095 airfoil case. Experimental data were not available for this set of parameters. The overall behavior of the force- and moment-coefficients looks similar compared to the previous case. But in detail some remarkable differences are present: Before the maximum lift is reached, some oscillations of the lift curve can be observed.

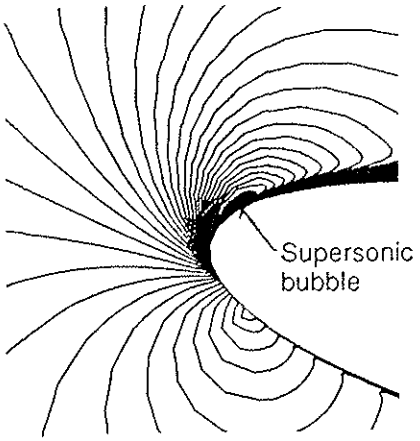

Fig. 4: Machnumber contours at NACA 23012, α = 21° upstroke.

This is caused by compressibility effects as will be demonstrated in the following section. The moment curve shows a very "peeky" behavior at high incidences. The stall vortex (vorticity contours) at the same angle α = 24.5° upstroke as in Fig. 2 is still more concentrated and attached to the airfoil: lift stall and specifically moment stall are shifted considerably to higher incidences.

4. Compressibility effects, laminar separation bubble.

The cases shown so far have been obtained for a Machnumber of the uncoming flow of Ma_∞ = 0.28. It is shown in ***Fig. 4*** that this low Machnumber of the undisturbed flow creates already a small supersonic bubble at the airfoil leading edge. The question arises, how the dynamic stall process is influenced, if Machnumber and/or Reynoldsnumber are considerably reduced. The following two subsections investigate these effects for the NACA 23012 and for the NACA 0012 airfoil sections.

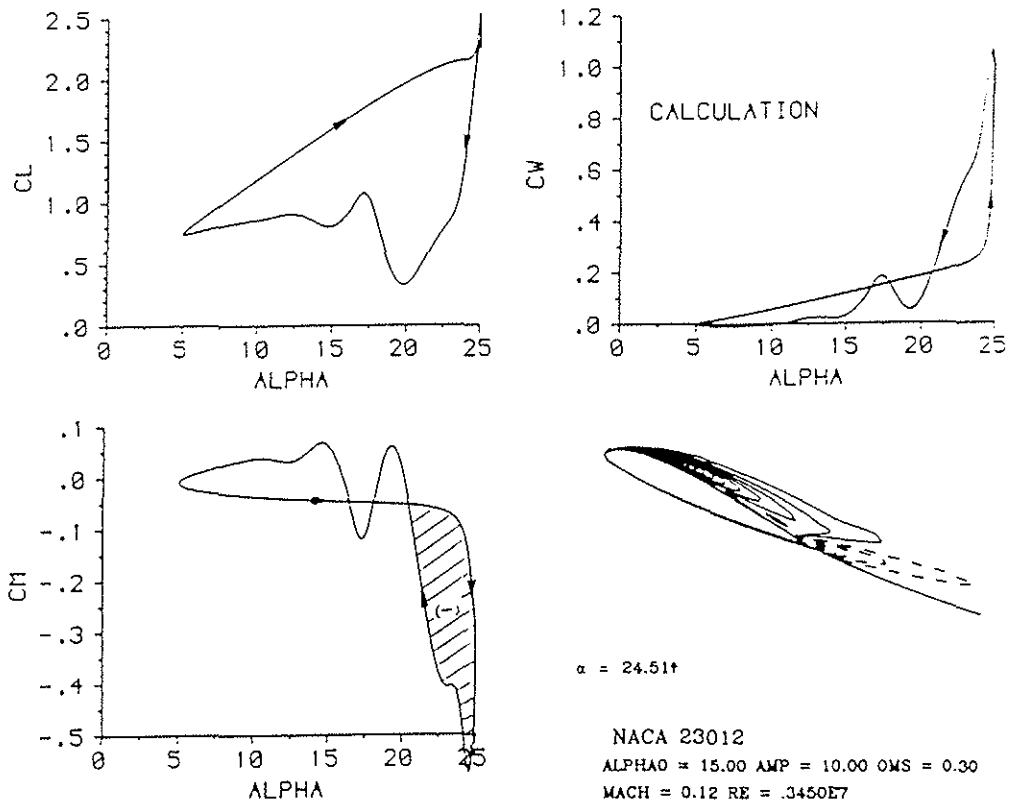

Fig. 5: Force- and moment-distributions for the NACA 23012 airfoil section: Ma_∞ = 0.12. Instantaneous vorticity distributions at α = 24.51° upstroke.

4.1 NACA 23012 airfoil.

Fig. 5 displays again lift, drag and moment distributions for the NACA 23012 airfoil section at Ma_∞ = 0.12. All other parameters remaine unchanged compared to Fig. 3. Several differences are observed between both cases: the lift-curve shows a steep increase beyond α_{max} = 25°, i.e. in the beginning of the downstroke. The moment-curve shows also a shift of moment stall to higher incidence (close to 25°). At downstroke however the moment-curve develops a hysteresis-loop (dashed area in Fig. 5) which corresponds to a strong ***negative damping*** in this incidence range.

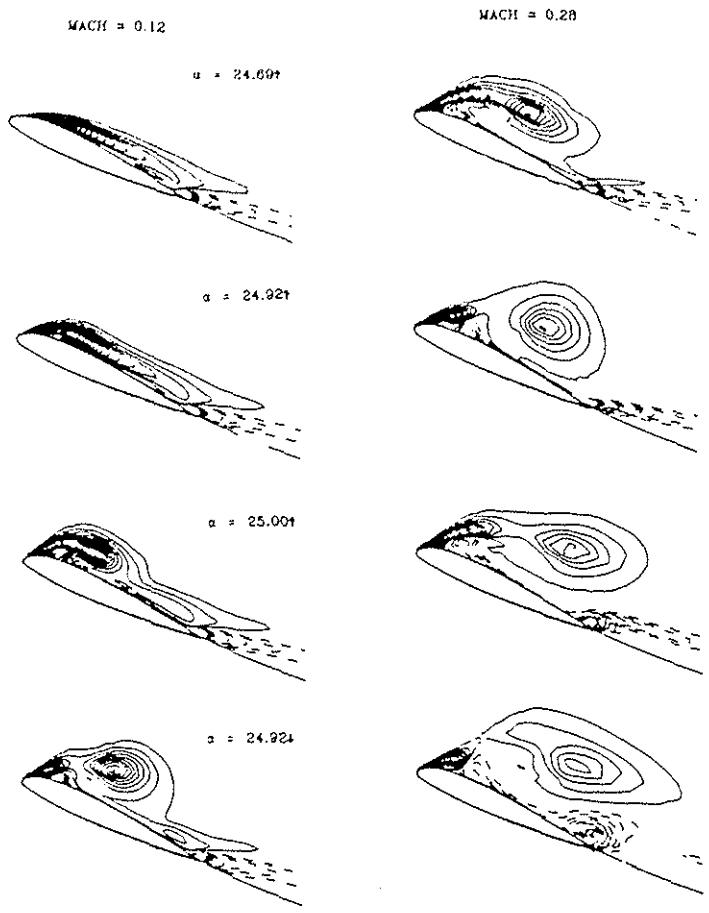

Fig. 6: NACA 23012: Vorticity contours at high incidence range, left: Ma_∞ = 0.12, right: Ma_∞ = 0.28.

Due to the small Re-number of 600 000 a laminar separation bubble starts to form beyond $\alpha = 6°$ in the experimental case which is not present in the calculation (fully turbulent). The separation bubble shifts the start of the dynamic stall process to earlier incidences ($\alpha = 12°$). *Fig. 8* shows calculated density contours at $\alpha = 13.68°$ upstroke where a similar behavior (start of the stall process) occurs compared to the experiment at $\alpha = 12°$. It seems that the separation bubble initiates the dynamic stall process at lower incidences. This is the same trend as found in the previous section due to an increase of Ma_∞ and the development of a supersonic bubble at the leading edge (Fig. 4).

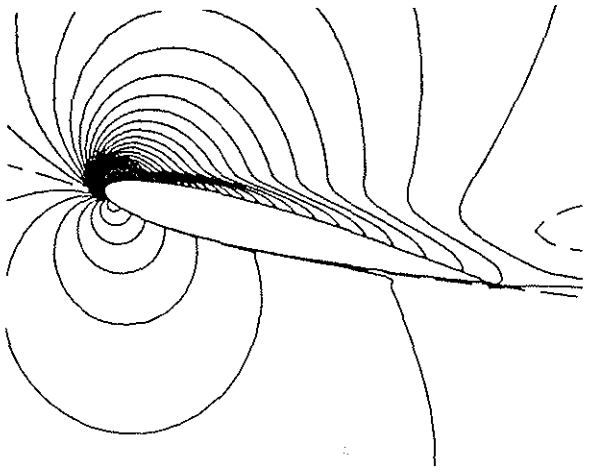

Fig. 8: NACA 0012: Density contours at α = 13.68 upstroke.

The vorticity distribution in Fig. 4 (again at $\alpha = 24.5°$ upstroke) shows as in the previous cases the concentration of vorticity downstream from the leading edge. But even at this high angle the flow is still attached.

Fig. 6 shows vorticity distributions for both Machnumber cases in detail within the range of maximal incidences. Compressibility is responsible for an earlier development and shedding of the stall vortex. Even at $\alpha = 24.9°$ downstroke the stall vortex is still attached to the airfoil surface for $Ma_\infty = 0.12$. It is completely seperated however for $Ma_\infty = 0.28$. In the latter case a counter-rotating vortex is already developing from the airfoils trailing edge.

4.2 NACA 0012 airfoil.

In [2] detailled flow investigations have been made for the NACA 0012 airfoil section under dynamic stall conditions by means of point diffraction interferometry. Emphasis was placed on the investigation of compressibility effects occuring during the beginning of the stall process. *Fig. 7* shows measured interferograms at four different incidences during upstroke compared to calculated density contours for the same case.

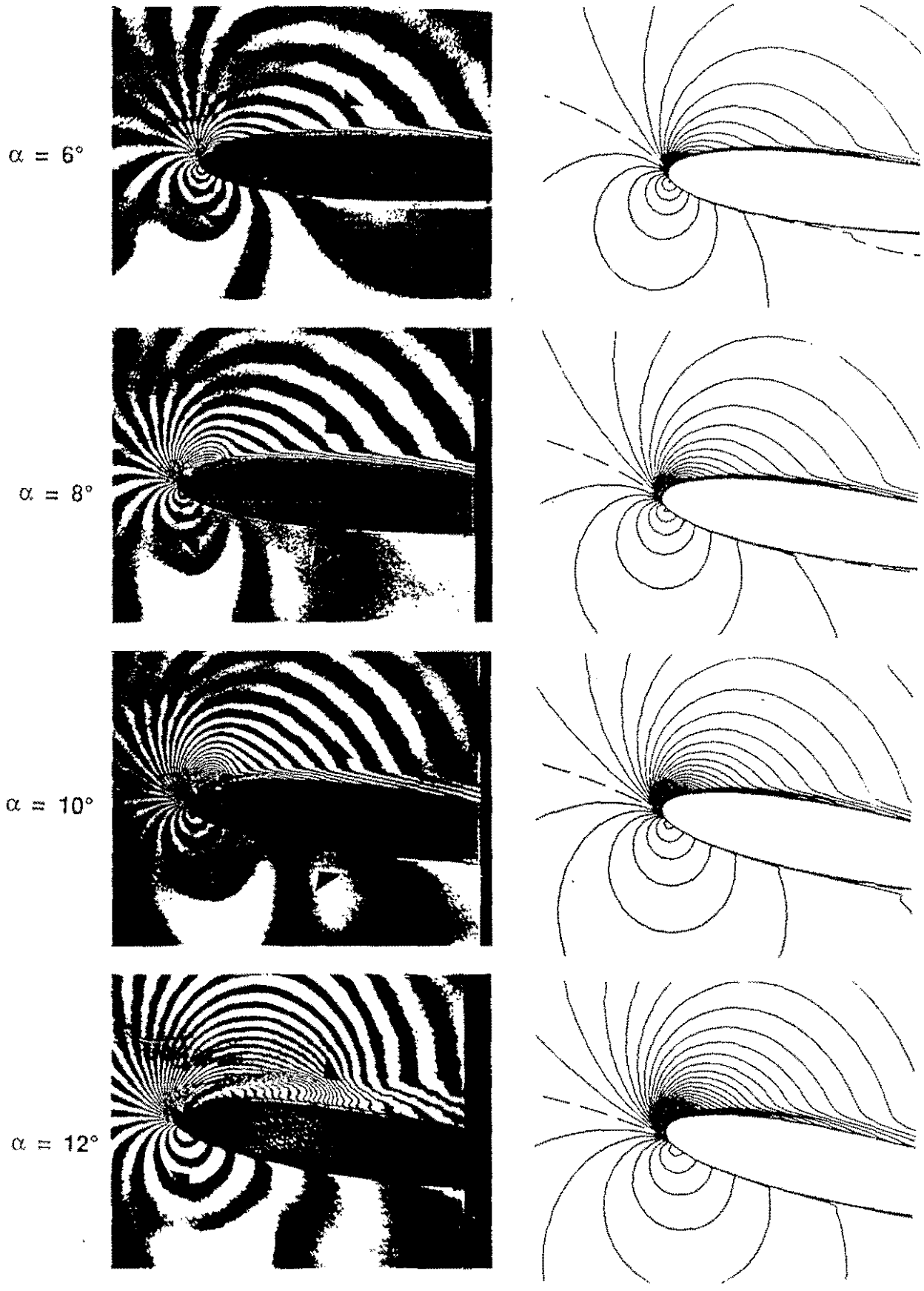

Fig. 7: NACA 0012: Interferograms, [3], versus calculated density contours, ($\Delta\rho$ = 0.1). $\alpha_0 = 10°, \alpha_1 = 10°, \omega^* = 0.1, Re = 600000$

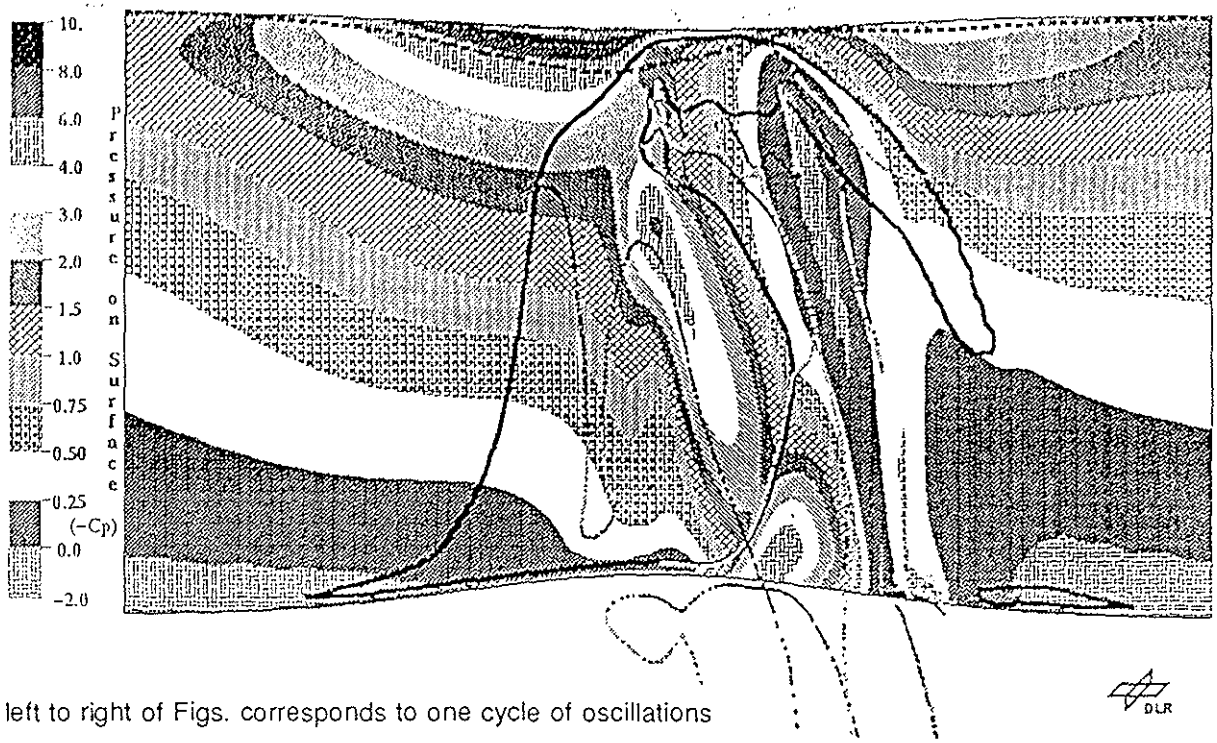

left to right of Figs. corresponds to one cycle of oscillations

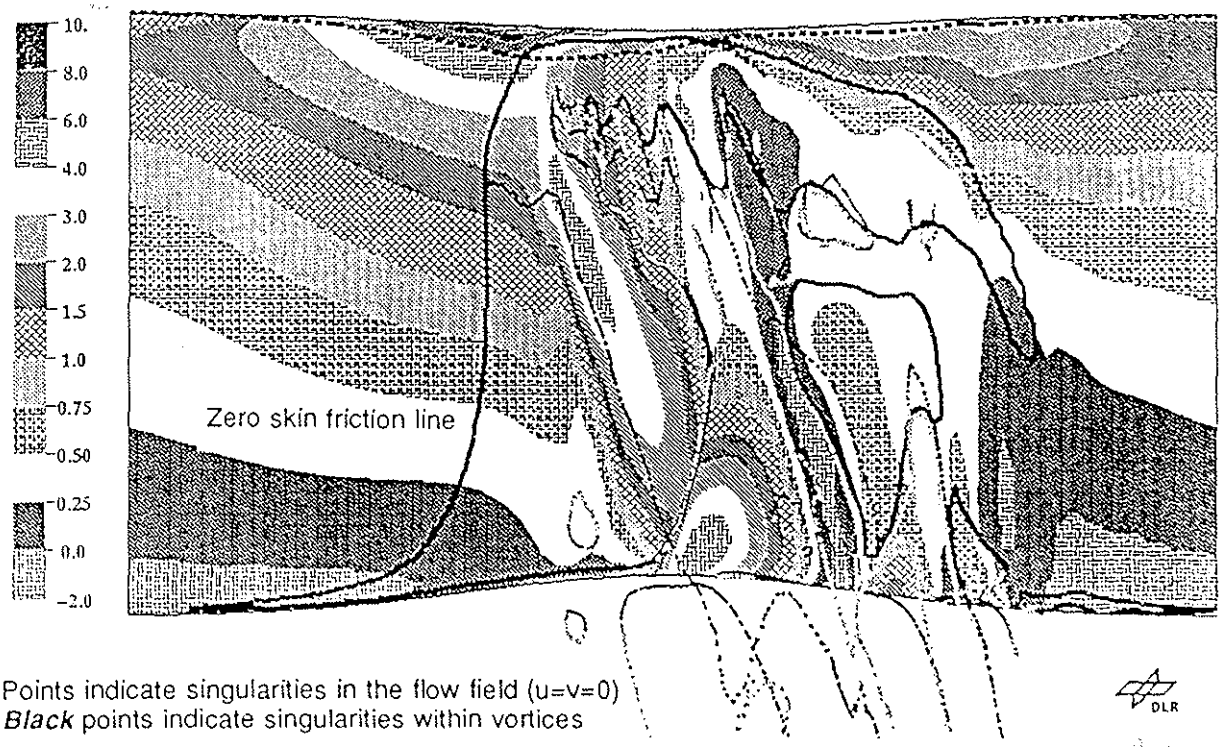

Points indicate singularities in the flow field (u=v=0)
Black points indicate singularities within vortices

Fig. 9: Pseudo-3d viewing: NACA 23012 airfoil, top: $Ma_\infty = 0.12$, bottom: $Ma_\infty = 0.28$.

5. Data visualization techniques.

In the previous sections most of the calculated data have been displayed in a conventional way, by plotting overall forces and moments as function of incidence or by instantaneous plots of vorticity, density etc. The unsteady separated flows on oscillating airfoils are extremely complex. To physically understand these flows, new means for display are necessary to better represent the ***unsteadyness*** of the flow. On the other hand the calculations produce a tremendeous amount of

informations: These data must be compressed in such a way that the important events are visable and ready for interpretation. New graphic software tools [12] have recently been developed in DLR with the ability and flexibility to do this important job.

5.1 Pseudo 3d-viewing.

One possibility to investigate the flow completely over a whole cycle of oscillation is a pseudo 3d-viewing, as displayed in Figs. 9. These Figures show flow events on the upper airfoil surface (NACA 23012) developing in time. The horizontal axis is the time-axis, the vertical axis (aligned with U_∞) represents the spatial dimension from airfoil leading (top) to trailing edge (bottom). The Figure shows a projection of the airfoil, therefore the chord is changing during the cycle. Both Figures show the pressure-distributions on the airfoil surface for $Ma_\infty = 0.12$ (Fig. 9, top) and $Ma_\infty = 0.28$ (Fig. 9, bottom) corresponding to the cases discussed in the previous sections. In addition lines of zero skin friction, singular points (black within vorticies),etc. are als included [13]. Several flow events can be observed from these Figures: Tongues of low pressure areas are developing from the leading edge along the chord as the effect of the dynamic stall vortex. A second pressure low develops at the airfoil trailing edge at a later time. The slope of the pressure low in space and time is a measure of the travel-velocity of the dynamic stall vortex. In both Machnumber cases this velocity is very similar. However the shedding event is shifted to later times in the low Machnumber case. Areas of reversed flow and poststall oscillations can be studied as well. This type of pseudo 3d-viewing can be varied in different ways, i.e. by display of other flow quantities. Such presentations may therefore serve as footprints of the unsteady seperated flows.

5.2 Video movie.

The other way to visualize unsteady numerical data is to do it directly by video movie. Much work has been done recently within a cooperation between the DLR-Institute of Fluid Mechanics and the Institut für den Wissenschaftlichen Film (IWF), Göttingen to develop video movies from calculated numerical data [7].

Within the scope of this cooperation the experts developing the numerical code and producing the data, the experts reducing these data effectively by graphical visualization tools and the experts on the "movie making" side worked close together. The product from this cooperation [7] shows different flow quantities like vorticity-, Machnumber-, pressure-fields as functions of time, direct comparisons of these quantities as time is progressing, focusing of flow fields where important effects develop and corresponding slow motions over parts of the oscillatory cycles, where flow events are of special interest.

Figs. 10 show as a special visualization technique time-lines of particles during the movement of the airfoil. Variing the colour of the instantaneous starting lines in an effective way the time-dependent development of the unsteady separated and vortical flows are made visible. A similar technique is applied in experimental fluid dynamics with the hydrogen bubble method.

Figs. 10 show two instantaneous flow fields represented by particles at the beginning (top) and the end (bottom) of the lift stall (see sketch of c_L *versus* α).

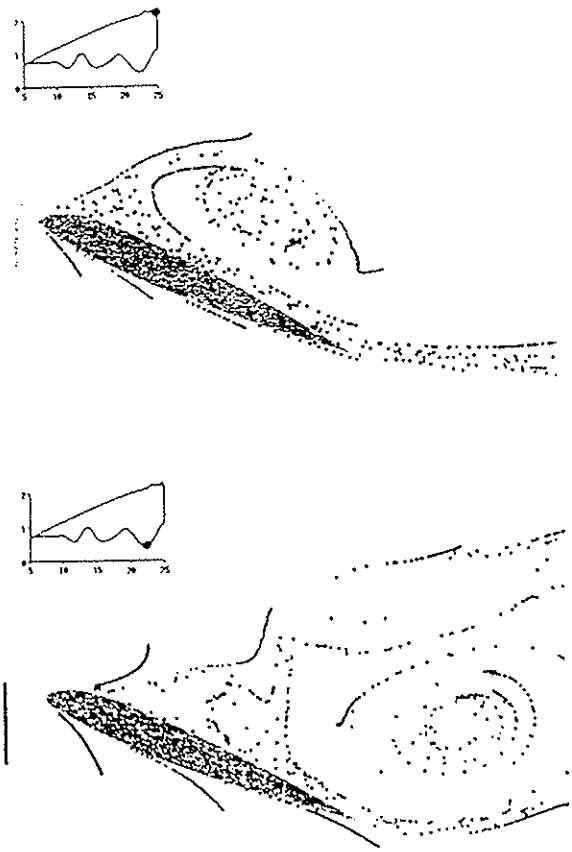

Fig. 10: NACA 23012: Development of time-lines.

6. Conclusions.

A numerical code has been developed based on the 2d-unsteady Navier-Stokes equations to calculate the viscous flow about helicopter airfoil sections. Emphasis was placed on the deep dynamic stall case including separation and vortex shedding from the airfoil surface. Comparisons of the numerical results with experimental data show good correspondance of the overall forces and moments. The large amount of data for all field quantities has been made visible by corresponding graphic tools recently developed in the DLR. Different visualization techniques, including pseudo 3d-viewing and the medium video movie have been applied successfully. Future work is necessary to simplify and accelerate the procedure from the calculation of the data to the final visualization product.

7. References.

[1]	McCroskey,W.J., McAllister,K.W., Carr,L.W., Pucci,S.L.	An Experimental Study of Dynamic Stall on Advanced Airfoil Sections. NASA TM 84245,July 1982,Vol. 1-3.
[2]	Carr,L.W., Chandrasekhara,M. S., Brock,N.J.	A Quantitative Study of Unsteady Compressible Flow on an Oscillating Airfoil. AIAA 22nd Fluid Dynamics, Plasma Dynamics & Lasers Conference. June 24-26, 1991, Honolulu, Hawaii.
[3]	Chandrasekhara,M. S., Ahmed,S.	Laser Velocimetry Measurements of Oscillating Airfoil Dynamic Stall Flow Field. AIAA-paper No. 91-1799. 22nd Fluid Dynamics, Plasma Dynamics & Lasers Conference. June 24-26, 1991, Honolulu, Hawaii.
[4]	Geissler,W., Carr,L.W., Cebeci,T.	Unsteady Separation Characteristics of Airfoils Operating under Dynamic Stall Conditions. 12th European Rotorcraft Forum, Sept. 22-25 (1986), Garmisch-Partenkirchen, Germany. paper No. 32.
[5]	Beam,R.W., Warming,R.F.	An Implicit Finite-Difference Algorithm for Hyperbolic Systems in Conservation-Law Form. J. of Comp. Physics 22, 87-110 (1976), pp. 87-100.
[6]	Pulliam,T.H.	Artificial Dissipation Models for the Euler Equations. AIAA J., Vol. 24, No. 12, Dec. 1986, pp. 1931-40.
[7]	Geissler,W., Vollmers,H., Grosse,H.	Dynamic Stall, Video Movie, 1992, VHS-Pal.
[8]	Geissler,W.	Instationäres Navier-Stokes Verfahren für beschleunigt bewegte Profile mit Ablösung. DLR-FB 92-03 (1992). Deutsche Forschungsanstalt für Luft-und Raumfahrt.
[9]	Sorensen,R.L.	Computer Program to Generate Two-Dimensional Grids about Airfoils and other Shapes by the use of Poissons Equation. NASA-TM-81190 (1981).
[10]	Chyu,W.J., Davis,S.S.	Numerical Studies of Unsteady Transonic Flow over an Oscillating Airfoil. AGARD CP 374, Sept. 1984, pp. 3.1-3.22.
[11]	McCroskey,W.J.	Unsteady Airfoils. Ann. Rev. Fluid Mech., 1982, pp. 285-311.
[12]	Vollmers,H.	The Recovering of Flow Features from Large Numerical Data Bases. Lecture Series on 'Comp. Graphics and Flow Visualization in CFD', VKI, Belgium, Sept. 16-20,1991
[13]	Vollmers,H. Kreplin,H.-P. Meier,H.U.	Separation and Vortical Type Flow around a Prolate Spheroid. - Evaluation of Relevant Parameters- Agard CP 342, Apr.1983, Rotterdam,Netherlands.